Supporting Information

Nanostructured Cobalt/Copper Catalysts for Efficient Electrochemical Carbon Dioxide Reduction

*Sharon Abner and Aicheng Chen**

Electrochemical Technology Centre, Department of Chemistry, University of Guelph, 50 Stone Road East, Guelph, Ontario N1G 2W1, Canada.

Experimental section

S1. Material characterization

The surface morphologies and compositions of the fabricated Co/Cu-based catalysts were studied using scanning electron microscopy (SEM, FEI Inspect S50) combined with energy dispersive X-ray (EDX) spectroscopy and analyzed using AZtech Spectrum software. The field emission SEM images of the Co/Cu catalysts were obtained using FE-SEM (FEI Quanta FEG 250 SEM). Images were collected at a working distance of 10.0 mm with a source bias of 20 keV. X-ray diffraction (XRD) patterns were recorded using a PANalytical Empyrean diffractometer with Cu $K\alpha_1$ radiation source (1.54060 Å). The signal was recorded between the 2θ angles of 20 to 90 degrees for 30 min per sample. XRD data were analyzed with X'Pert High Score Plus software. X-ray photoelectron spectroscopy (XPS) was performed with a Thermo Scientific K-α XPS spectrometer at a take-off angle of 90° (relative to the surface) using a monochromatic Al Kα X-ray source ($h\nu$ = 1486.6 eV). All data processing was done using CasaXPS software. All the XPS spectra were referenced to the C 1s binding energy of 284.8 eV and fitted using Shirley baselines. The high-resolution spectra of Co 2p and Cu 2p were curve-fitted following the procedure outlined in Biesinger et al. [1–3] Before each of the mentioned characterization techniques, the catalysts were electrochemically reduced (EC treated) and were left to dry overnight in a vacuum oven (Thermo Scientific) at 80°C and approximately 28-inch Hg (948 mbar).

S2. Electrochemical characterization

Metrohm Autolab Potentiostat was used in obtaining the electrochemical results (e.g., linear sweep voltammetry (LSV) and chronoamperometry (CA)) in a two-compartment cell system. A freshly

prepared 3×1 cm^2 Ti/Ta_2O_5-IrO_2 was used as the counter electrode, as described in previous work.[4] The Ti/Ta_2O_5-IrO_2 was used instead of the conventional Pt electrode to improve the stability and reproducibility of the electrochemical measurements. The counter electrode was separated from the working and reference electrodes in an H-cell configuration using an anionic exchange membrane (AMI-7001 Membranes International Inc.). Ag/AgCl (3.0 M KCl) was used as the reference electrode and the measured potential was converted to the reversible hydrogen electrode (RHE) scale (E vs. RHE) using the following equation:

$$E\ (vs.RHE) = E\ (vs.\ Ag/AgCl) + 0.0591\ V \times pH + 0.210\ V \quad \text{(S1)}$$

A CO_2-saturated 1 M KOH solution was used as the electrolyte for all the CO_2RR experiments. The pH of the electrolyte dropped to 8.00 after 15 min of purging with CO_2 gas (according to equation S2)[5,6] and the pH was measured consistently before and after each CO_2RR experiment.

$$CO_2 + OH^- \rightleftarrows HCO_3^- \quad \text{(S2)}$$

For comparison, the fabricated catalysts were also tested for the hydrogen evolution reaction (HER). HER measurements were conducted in the same electrochemical cell as the CO_2 reduction experiments, but the electrolyte solution was changed to Ar-saturated 0.5 M K_2SO_4 with an adjusted pH of 8.00. To examine the trends in electrode activity in different pH levels, the LSVs were repeated in a CO_2-saturated 0.5 M K_2SO_4 with pH 6.7 and were compared to those obtained in Ar-saturated 0.5 M K_2SO_4, where the pH was also adjusted to 6.7. The current efficiencies were calculated using the following equation:

$$Current\ efficiency\ \% = \frac{(j_{CO_2RR} - j_{HER})}{j_{CO_2RR}} \times 100 \quad \text{(S3)}$$

where j_{CO_2RR} is the current density recorded during CO_2RR and j_{HER} is the current density recorded during HER.

S3. Reduction product analysis

Gas and liquid products of the electrochemical reduction of CO_2 were collected in a two-compartment cell with an anionic exchange membrane (AMI-7001 Membranes International Inc.) to prevent the reduction products from being oxidized on the counter electrode. The working and reference electrodes (Ag/AgCl, 3 M KCl) were placed in a gas-tight cathode compartment in which gas products accumulated. The 1 M KOH electrolyte was continuously purged with CO_2 gas through a side gas inlet. 3×1 cm^2 Ti/Ta_2O_5-IrO_2 counter electrode was placed in the anode cell compartment. Gas chromatography (GC) was employed for analyzing the gas products generated from the CO_2RR electrochemical cell directly. The Multiple-gas-#5, SRI GC Instrument was equipped with 3' MS5A/6' & 18' Hayesep D columns, flame ionization detector (FID), and thermal conductivity detector (TCD). The detectors were calibrated using standard volumes of hydrogen (H_2) or carbon monoxide (CO) using helium as the gas carrier. The following equation was used to calculate the Faradaic efficiency of CO in the gas samples:

$$FE_{CO} = \frac{Q_{CO}}{Q_{total}} = \frac{(zPVx_{CO}F)/RT}{\int_0^t Idt} \quad \text{(S4)}$$

Where z is the number of electrons involved in the reduction reaction ($2e^-$ for CO production), P is pressure (101 kPa), V is the total volume of the headspace (20.0 mL), x_{CO} is the volume fraction of the gas in the headspace of the GC instrument determined by the CO calibration curve, F is the Faraday constant (96485 C/mol), R is the gas constant (8.314 J/mol K), T is the temperature (298 K), Q_x is the partial charge (C) required to produce product CO, Q_{total} is the total charge that passes through the electrochemical cell (C), I is the current measured by the cell (A), and t is the time in which the current was measured (s).

To identify and quantify the liquid products, a 600 MHz Bruker Avance III NMR with a Cryoprobe was employed to record the ^{1}H NMR spectra. 350 µL of the liquid reduction-products sample was mixed with 350 µL internal standard of 0.05 wt. % tetramethylsilane (TMS) in D_2O. The following equation was used to calculate the Faradaic efficiency of formate ions ($HCOO^-$) in the liquid samples:

$$FE_{formate} = \frac{Q_{formate}}{Q_{total}} = \frac{z\, n_{formate}\, F}{\int_0^t Idt} \quad \text{(S5)}$$

Where $n_{formate}$ is the number of moles of formate determined by the formate calibration curve, z is the number of electrons involved in the reduction reaction ($2e^-$ for $HCOO^-$ production), F is the Faraday constant (96485 C/mol), $Q_{formate}$ is the partial charge (C) required to produce the formate, Q_{total} is the total charge that passes through the electrochemical cell (C), I is the current measured by the cell (A), and t is the period in which the current was measured (s).

S4. Electrochemically active surface area (EASA) determination

To determine the electrochemically active surface area (EASA) of the fabricated catalysts, the double-layer capacitances (C_{DL}) were measured and divided by the specific capacitance (C_S) of an atomically smooth cobalt surface under identical electrolyte conditions, this ratio is defined as the surface roughness factor (Rf). Then, R_f is multiplied by the geometric area of the electrode (S = 1.00 cm^2) to get the EASA:

$$R_f = \frac{C_{DL}}{C_S} \quad \text{(S6)}$$

$$EASA = R_f\, S \quad \text{(S7)}$$

The double-layer charging/discharging current density (Δj) is equal to the scan rate (υ) multiplied by the double-layer capacitance (C_{DL}) as follows:

$$\Delta j = \upsilon\, C_{DL} = j_a - j_c \quad \text{(S8)}$$

Δj is the current density difference between the anodic (j_a) and cathodic (j_c) current densities at a chosen potential. Thus, by plotting the measured Δj versus scan rate, the double-layer capacitance can be calculated from the slope of the linear plot. Cyclic voltammograms (CVs) were obtained at

various scan rates (10 – 100 mV/s) in a narrow potential window (0.00 – 0.20 V vs. RHE), where no Faradaic reaction was observed. CVs were recorded in a 1 M KOH electrolyte (pH 8.00) using a three-electrode system in a one-compartment cell. Purging with CO_2 gas was stopped after the pH of the electrolyte reached 8.00. The specific capacitance (C_S) of a smooth cobalt surface was measured similarly. EASA-corrected LSVs of Co/Cu - A (turquoise), and Co/Cu – AA (orange) electrodes (Figure S4) were generated by dividing the geometric current density (mA/cm^2) measured during HER and CO_2RR experiments by the corresponding EASA value (Table S1). The EASA correct current density (j_{EASA}) was then plotted versus the applied potential.

$$j_{EASA} = \frac{j}{EASA} \tag{S9}$$

S5. In situ electrochemical FTIR study

The *in situ* attenuated total reflection Fourier transform infrared (ATR – FTIR) spectroscopic study was conducted in an external reflection configuration (also known as Otto configuration),[7,8] as shown in the supporting information (Scheme S1). In this configuration, the working electrode coated with the fabricated catalyst was placed against the light-guiding crystal with a high refractive index (ZnSe hemisphere window, n = 2.42) and effectively trapping a thin layer of electrolyte (approximately 10 μm thickness) between itself and the crystal. This approach allows the detection of both adsorbed species and electrolyte species trapped in the thin layer. These experiments were carried out using an 8700 Nicolet Fourier transform infrared spectrometer with a liquid N_2-cooled HgCdTe (MCT) detector and an incident angle of 30° with respect to the surface normal. A Ti rod was used as a holder to which the fabricated catalyst was attached at the bottom facing the ATR crystal. 3×1 cm^2 Ti/Ta_2O_5-IrO_2 was used as the counter electrode and Ag/AgCl (3.0 M KCl) was used as the reference electrode. To avoid interference from existing bicarbonate/carbonate species, 0.5 M K_2SO_4 solution was used as the electrolyte made with D_2O. For spectral clarity, the D_2O bending mode peak at 1200 cm^{-1} was subtracted from the spectra. For the CO_2RR experiments, the electrolyte was purged with CO_2 gas for 20 min before the start of the experiment and was continuously purged during the experiment. To monitor changes in signal intensity due to consumed or produced species, as well as to minimize spectral background, a subtractively normalized interfacial FTIR spectroscopic (SNIFTIRS) method was employed. In this method, spectra were acquired at base potential (E_1) and sample potential (E_2) and their difference was divided by the base spectrum at E_1 as follows:

$$\frac{\Delta R}{R} = \frac{[R(E_2) - R(E_1)]}{R(E_1)} \tag{S10}$$

where $R(E_1)$ and $R(E_2)$ are the reflection spectra at the applied potentials E_1 and E_2, respectively. The resulting spectrum is reported as a relative change in electrode reflectivity ($\frac{\Delta R}{R}$) as a function of wavenumber (cm^{-1}). In this study, the base spectrum ($R(E_1)$) was obtained at 0.0 V vs. RHE while the sample spectrum ($R(E_2)$) was collected at each -0.1 V potential step between -0.1 to -0.9 V vs. RHE with a spectral resolution of 4 cm^{-1}. According to Equation S8, a negative-oriented

peak appears if ($R(E_2)$) is greater than ($R(E_1)$). That is the case when a new species is being produced and detected in the sample spectrum at the applied potential E_2. However, a positive-oriented peak is observed when ($R(E_1)$) is greater than ($R(E_2)$). That happens when the detected species is consumed at the sample potential E_2.

To make sure that the thin layer of electrolyte trapped between the catalyst and the ATR crystal is refreshed, the working electrode was pulled away from the ATR window between experiments, and the CO_2-saturated electrolyte was allowed to mix. Time-dependent experiments were conducted in the following order: (1) the 0.5 M K_2SO_4 electrolyte was continuously purged with CO_2 gas during the experiment; (2) the working electrode with the Co/Cu-A or Co/Cu-AA catalyst was lowered to the ZnSe crystal, such that approximately 10 μm of a thin layer of electrolyte is trapped between the catalyst and the ATR-window; (3) The base potential (0 V vs. RHE) was applied for 10 s while a reference spectrum ($R(E_1)$) was taken (average of 8 scans); and (4) E_2 potential was applied for 100s while 20 spectra were collected (8 scans each). It takes 4 seconds to collect 8 scans with a 1 s delay between spectra. Thus, the time-dependent experiments present changes in vibrational bands from the time E_2 was applied, 0 s to 100 s, with 5 s intervals. Potential-dependent experiments were conducted in the following order: (1) the 0.5 M K_2SO_4 electrolyte was continuously purged with CO_2 gas during the experiment; (2) the working electrode with the Co/Cu-A or Co/Cu-AA catalyst was lowered to the ZnSe crystal; (3) the base potential (0 V vs. RHE) was applied for 100 s while a reference spectrum ($R(E_1)$) was taken (average of 64 scans); (4) -0.1 V vs. RHE (E_2) potential was applied for 100s while one spectrum was collected (average of 64 scans); (5) the electrode was raised again to refresh the electrolyte and then lowered again; and (6) -0.2 V vs. RHE was applied for 100 s while a spectrum was collected.

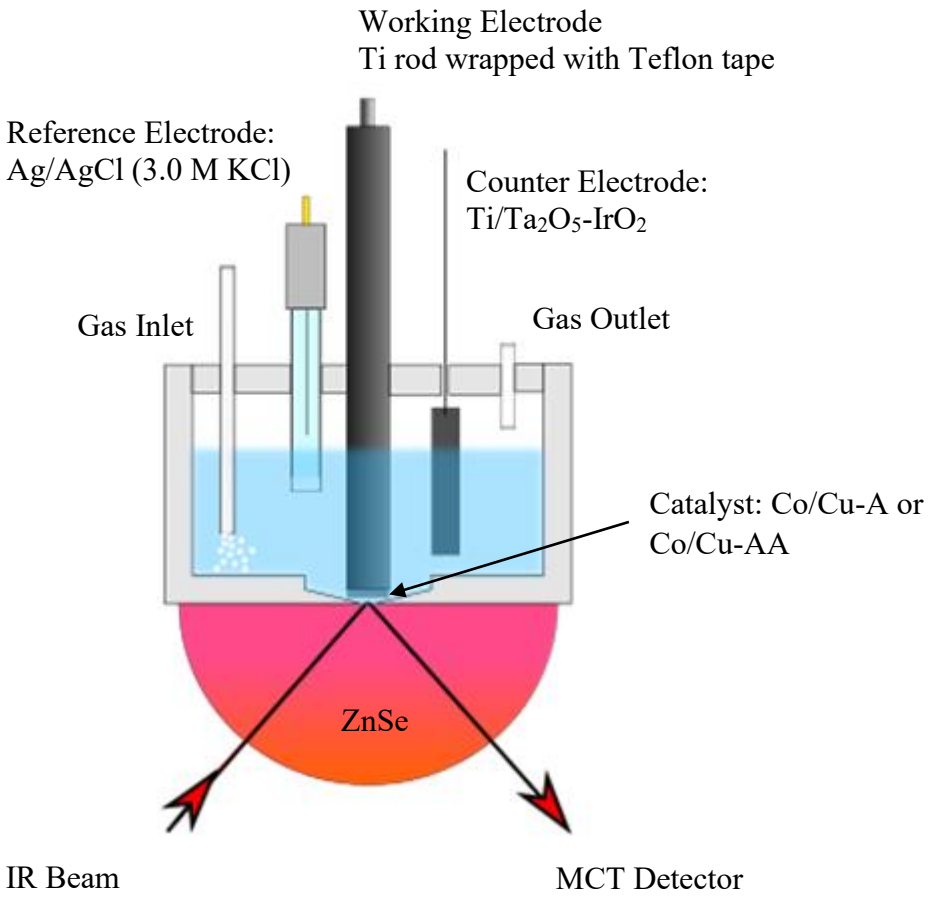

Scheme S1. Schematics of the *in situ* Electrochemical FTIR cell used in this study.

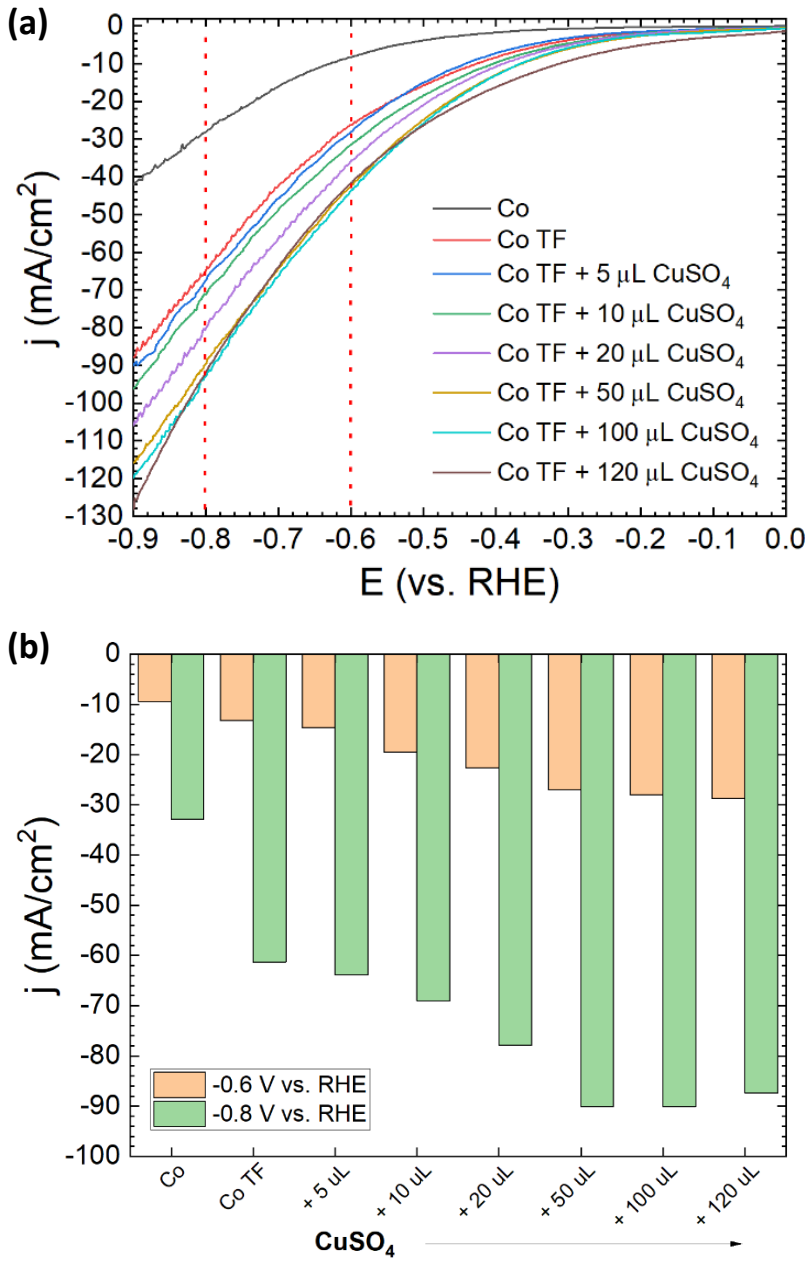

Figure S1. (a) LSVs of Co plate, Co TF, and Co TF drop-casted with 5 to 120 µL of 0.1 M $CuSO_4$ solution recorded at 20 mV/s scan rate. CO_2RR experiments were conducted in CO_2-saturated 1 M KOH (pH 8.0); (b) bar graph summary of the measured current densities measured during CA at -0.6 V and -0.8 V vs. RHE for 600 s using the electrodes presented in Figure S1a.

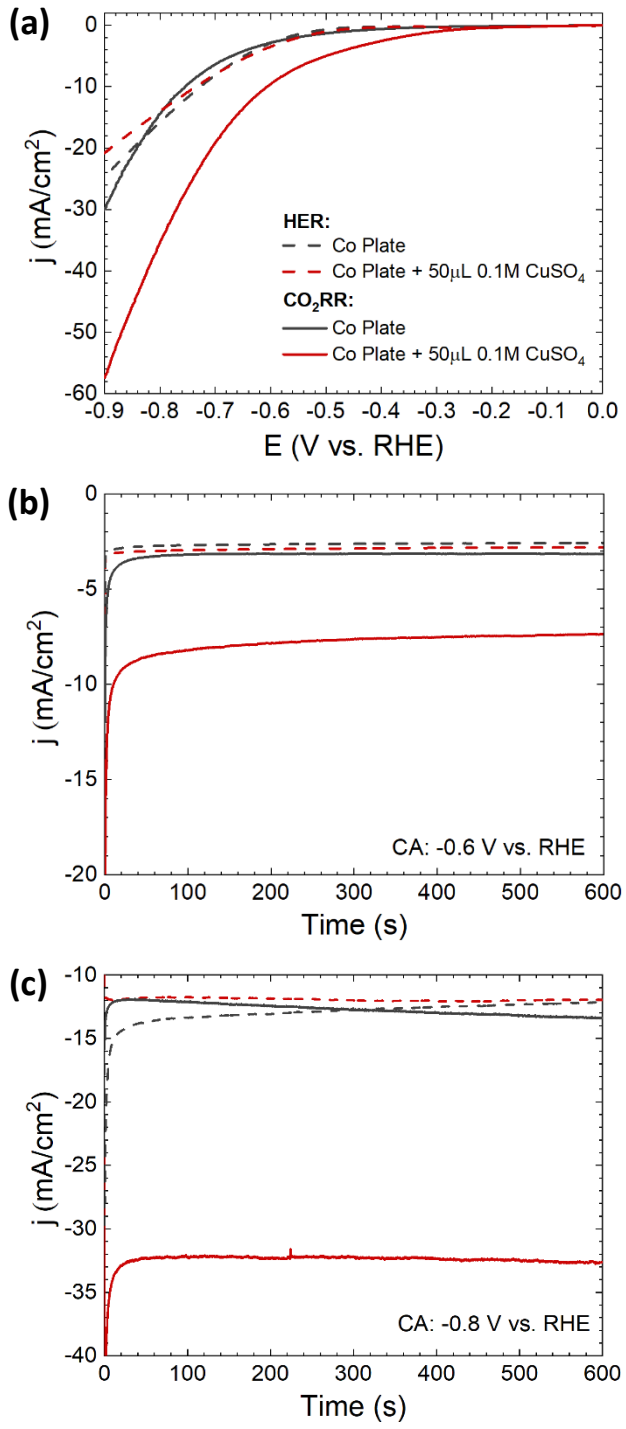

Figure S2. (a) LSVs of Co plate and Co plate + 50 μL 0.1 M $CuSO_4$ recorded at 20 mV/s scan rate. Dashed lines represent HER experiments conducted in Ar-saturated 0.5 M K_2SO_4 (adjusted pH 8.0) and solid lines represent CO_2RR experiments conducted in CO_2-saturated 1 M KOH (pH 8.0); (b) corresponding CA profiles of the electrodes measured at -0.6 V vs. RHE for 600 s; and (c) corresponding CA profiles of the electrodes measured at -0.8 V vs. RHE for 600 s.

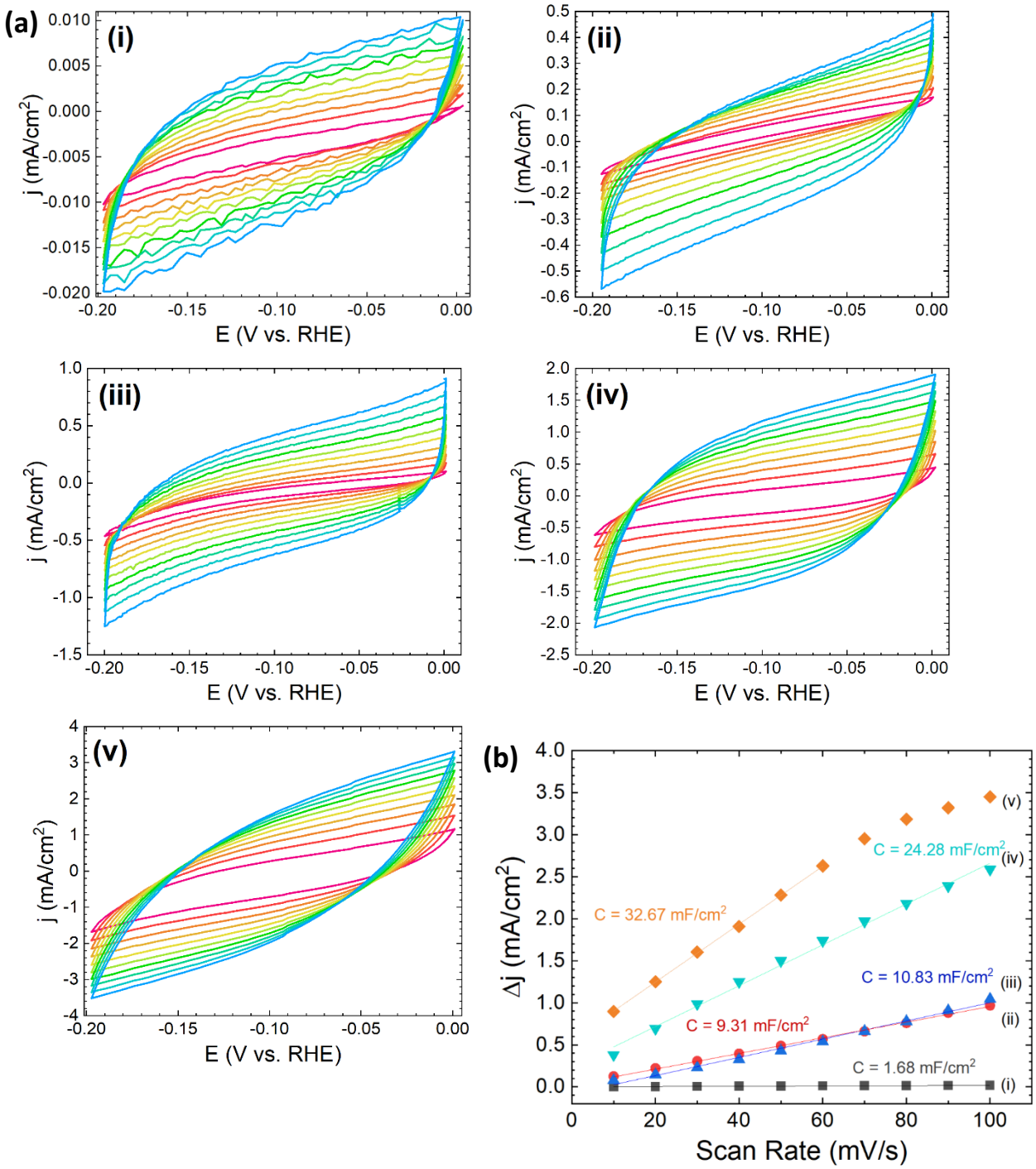

Figure S3. (a) Cyclic voltammograms of (i) Co substrate, (ii) Co TF, (iii) Co TF + 0.1 M $CuSO_4$, (iv) Co/Cu – A, and (v) Co/Cu – AA catalysts at scan rates 10 – 100 mV/s; (b) the calculated gap between the cathodic and anodic current densities (Δj) at -0.10 V vs. RHE plotted against the applied scan rate for (i) Co substrate, (ii) Co TF, (iii) Co TF + 0.1 M $CuSO_4$, (iv) Co/Cu – A, and (v) Co/Cu – AA.

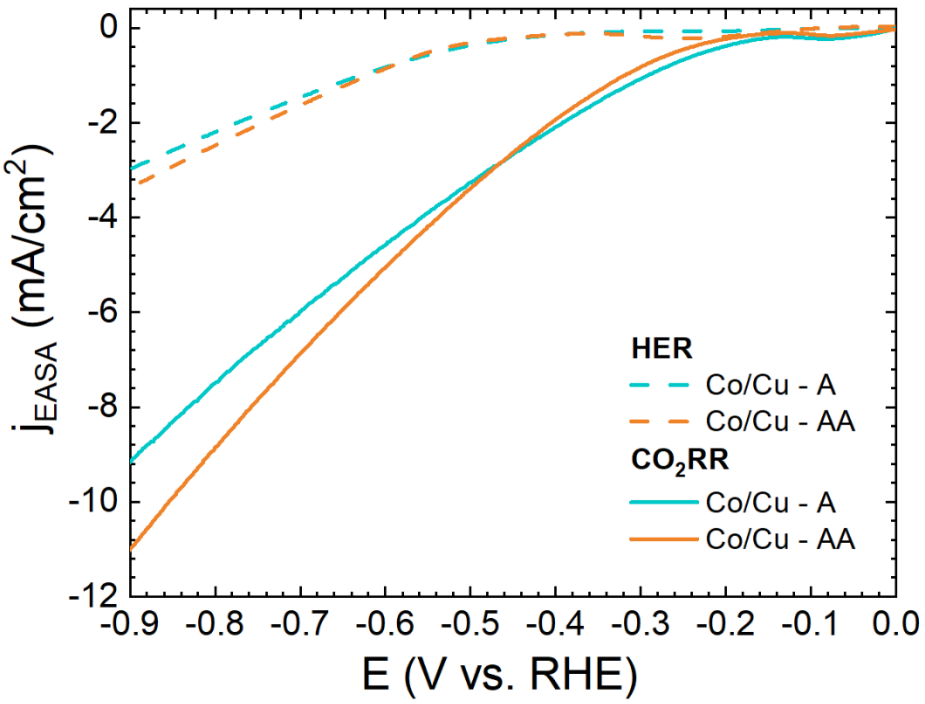

Figure S4. EASA-corrected LSVs of Co/Cu - A (turquoise), and Co/Cu – AA (orange) electrodes were recorded at a 20 mV/s scan rate. LSVs were collected at two conditions: dashed lines represent HER experiments conducted using Ar-saturated 0.5 M K_2SO_4 with adjusted pH 8.0, and solid lines represent CO_2RR experiments conducted in CO_2-saturated 1 M KOH (pH 8.0).

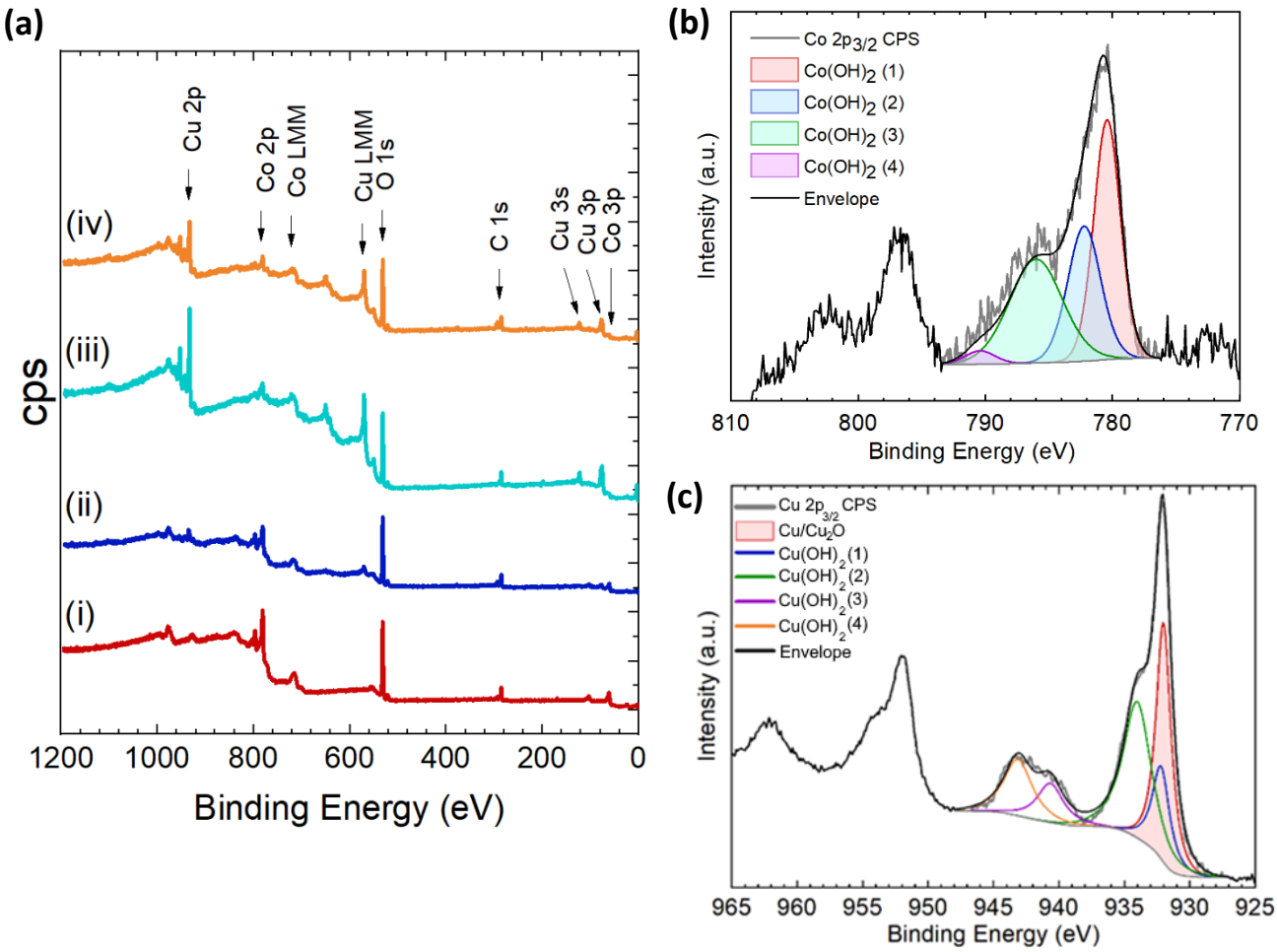

Figure S5. (a) XPS survey spectra of (i) Co TF, (ii) Co TF + 0.1 M $CuSO_4$, (iii) Co/Cu – A, and (iv) Co/Cu – AA; (b) high-resolution Co 2p XPS spectrum and curve-fitting results of Co/Cu – AA; (c) high-resolution Cu 2p XPS spectrum and curve-fitting results of Co/Cu – AA.

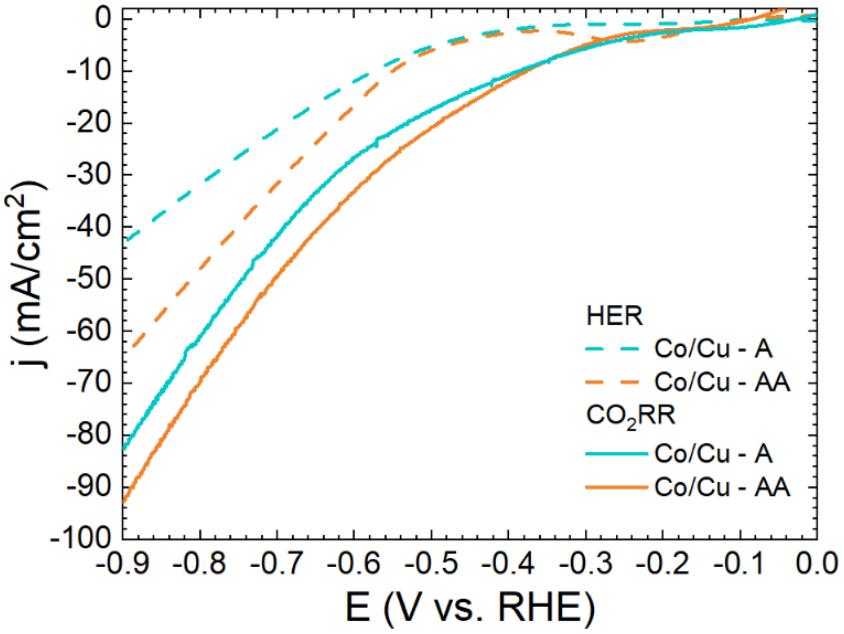

Figure S6. Linear sweep voltammograms of Co/Cu – A (turquoise), and Co/Cu – AA (orange) electrodes were recorded at a 20 mV/s scan rate. LSVs were collected at two conditions: dashed lines represent HER experiments conducted using Ar-saturated 0.5 M K_2SO_4 with adjusted pH 6.7, and solid lines represent CO_2RR experiments conducted in CO_2-saturated 0.5 M K_2SO_4 (pH 6.7).

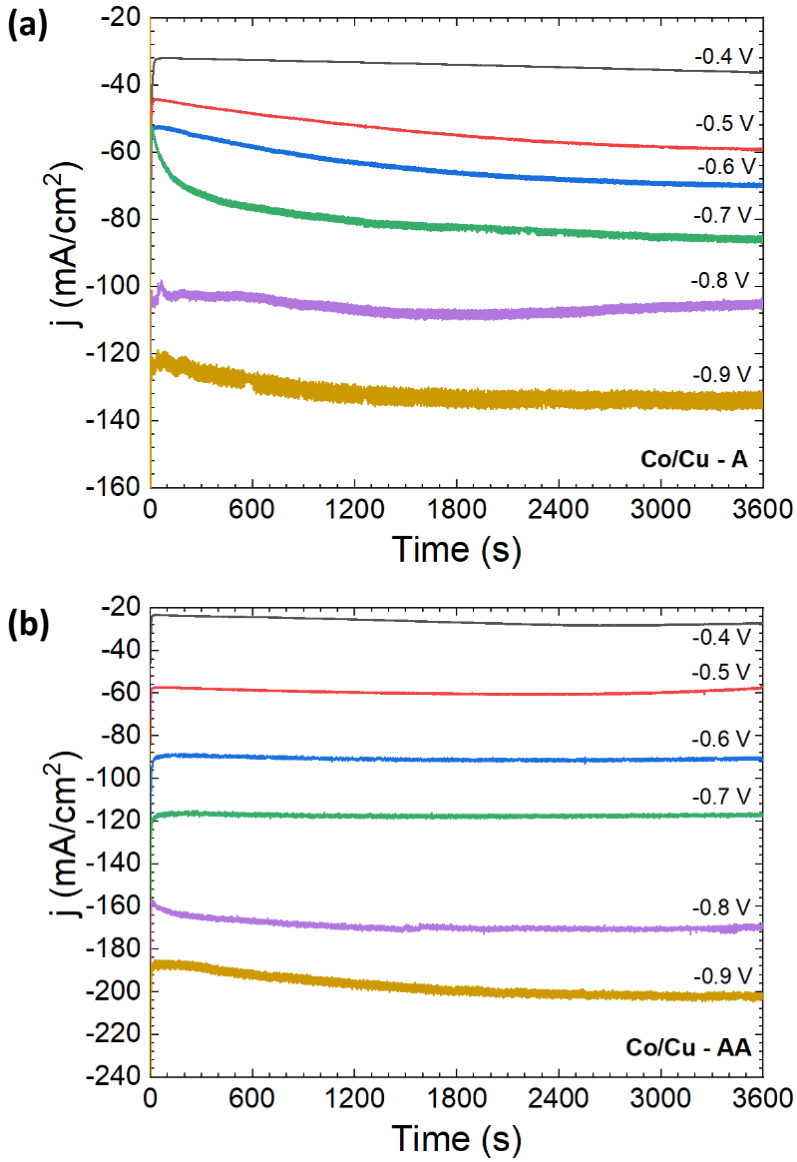

Figure S7. CA of (a) Co/Cu – A and (b) Co/Cu – AA at potentials -0.4 V to -0.9 V vs. RHE for 1 hour in a CO_2-saturated 1 M KOH (pH 8.00). The liquid products were collected to determine the formate Faradaic efficiencies and gas products were collected to determine CO Faradaic efficiencies.

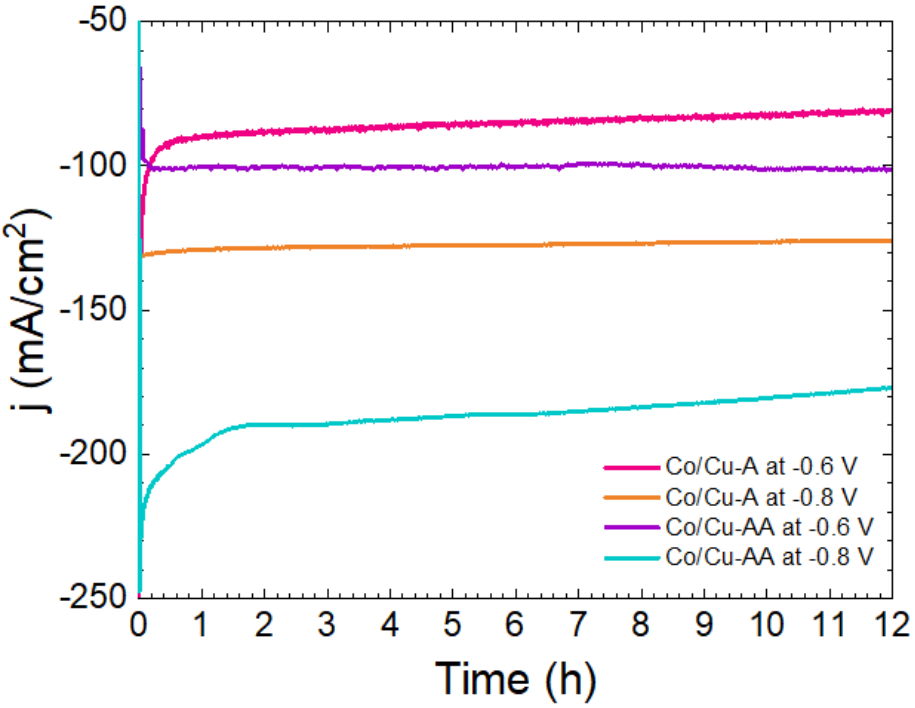

Figure S8. CA of Co/Cu – A and Co/Cu – AA at -0.6 V and -0.8 V vs. RHE for 12 hours in a CO_2-saturated 1 M KOH.

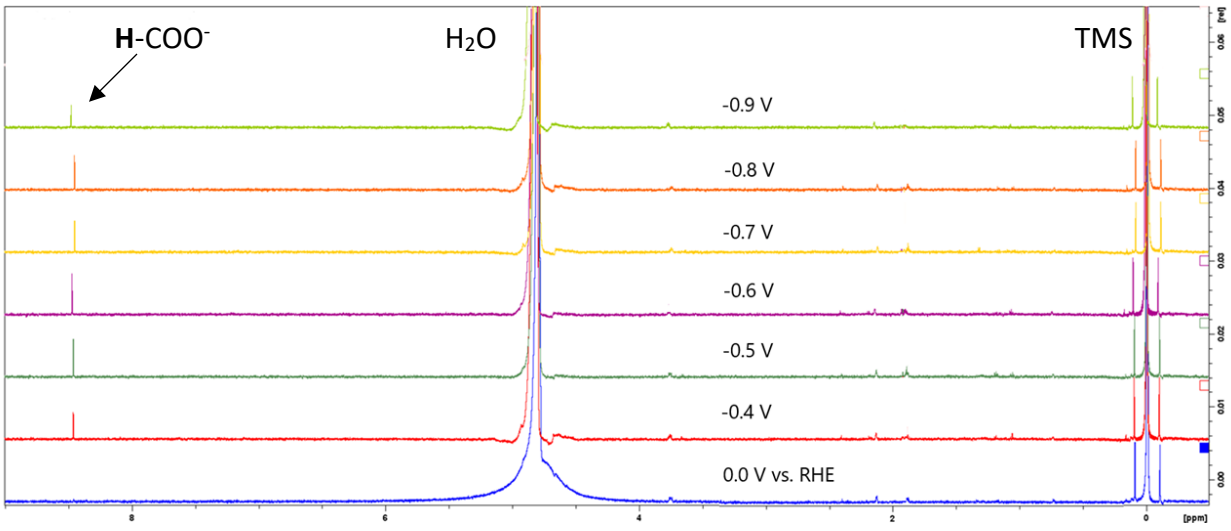

Figure S9. [1]H-NMR spectra of the liquid products obtained after 60 min of CO_2RR at applied potentials of 0.0 V and -0.4 to -0.9 V vs. RHE using Co/Cu – AA catalyst.

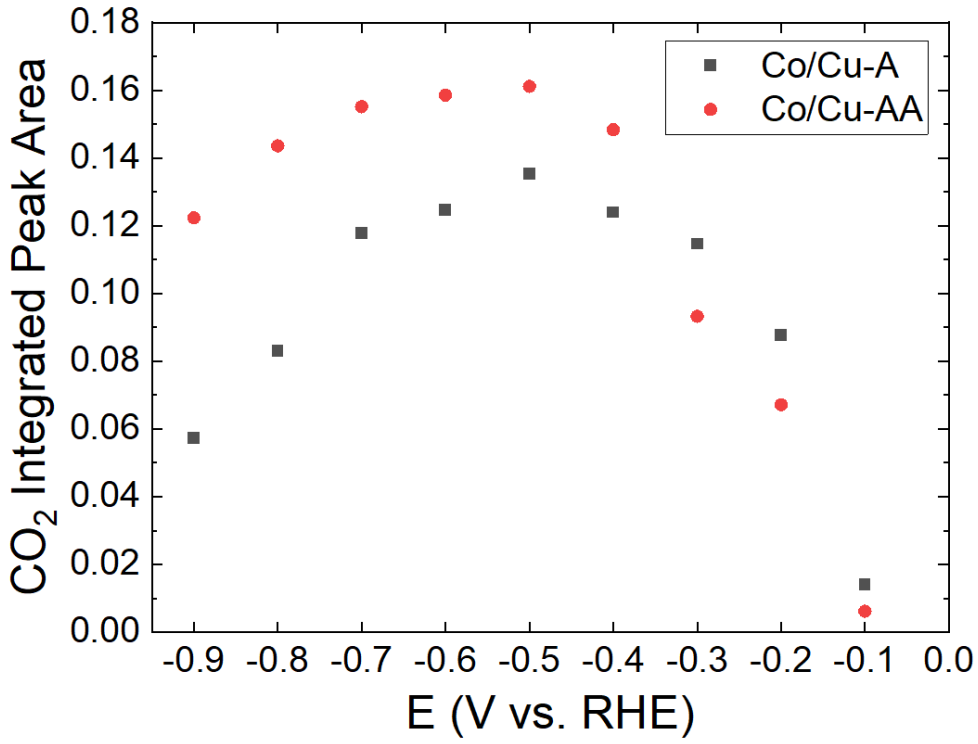

Figure S10. Integrated areas of the CO_2 peaks ($\nu_{as}(CO_2)$) from Figures 5a and Figure 5d during CO_2RR using Co/Cu – A (black) and Co/Cu – AA (red) catalysts, as a function of the applied potential.

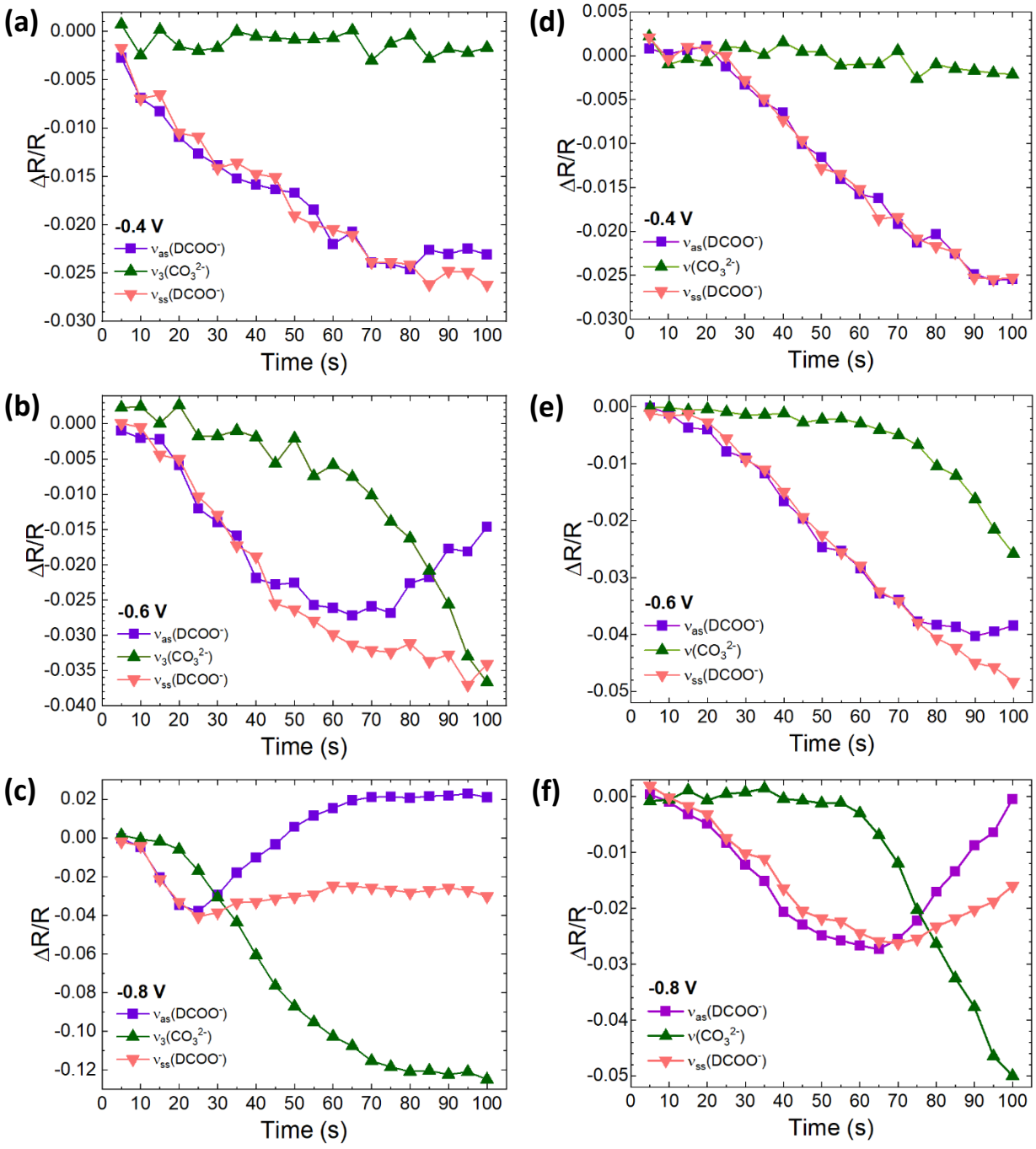

Figure S11. Absolute values of the corresponding peak intensities from Figure 6a and Figure 6b as a function of time recorded during the CO_2RR using (a–c) Co/Cu – A catalyst at potentials (a) -0.4 V, (b) -0.6 V, and (c) -0.8 V vs. RHE; and (e – f) Co/Cu – AA catalyst at potentials (d) -0.4 V, (e) -0.6 V, and (f) -0.8 V vs. RHE.

Table S1. Calculated capacitance values and electrochemically active surface area of the different nanostructured Co electrodes using CV.

Electrode	**Capacitance (mF/cm^2)**	**R^2**	**EASA (cm^2)**
(i) Co substrate	1.68	0.998	1.00
(ii) Co TF	9.31	0.999	5.54
(iii) Co TF + 0.1 M $CuSO_4$	10.83	0.996	6.45
(iv) Co/Cu – A	24.28	0.997	14.5
(v) Co/Cu – AA	32.67	0.998	19.4

Table S2. Atomic percentages of cobalt, copper, and oxygen atoms in the Co/Cu catalysts as determined by EDX.

Atomic %	**Co**	**Cu**	**O**
Co substrate	98.0	0.0	2.0
(i) Co TF	95.0	0.0	5.0
(ii) Co TF + 0.1 M $CuSO_4$	28.8	68.6	2.6
(iii) Co/Cu – A	12.7	76.2	11.1
(iv) Co/Cu – AA	11.4	73.4	15.2

Table S3. XRD (*hkl*) peak assignments, 2θ angles, relative intensities (%), corresponding species, and phases.

	h	k	l	2 θ (degrees)	I (%)	Species	Phases
(i) Co Plate	1	0	0	41.9	6.8	Co	hcp*
	0	0	2	44.5	77.2	Co	
	1	0	1	47.4	100.0	Co	
	1	1	0	75.8	0.1	Co	
(ii) Co TF	1	0	0	42.0	60.0	Co	hcp
	0	0	2	44.7	0.1	Co	
	1	0	1	47.8	100.0	Co	
	1	1	0	76.2	33.5	Co	
(iii) CoTF + 50 µL of 0.1 M Cu_SO_4	1	0	0	41.7	100.0	Co	hcp
	1	1	1	43.5	69.5	Cu	fcc**
	0	0	2	44.6	8.9	Co	hcp
	1	0	1	47.5	45.3	Co	hcp
	0	0	2	50.6	3.9	Cu	fcc
	0	2	2	74.5	38.3	Cu	fcc
(iv) Co/Cu – A	2	2	0	31.6	18.1	Co_3O_4	cubic
	3	1	1	37.2	100.0	Co_3O_4	cubic
	1	1	1	37.2	100.0	Cu_2O	cubic
	4	0	0	42.8	54.6	Co_3O_4	cubic
	2	0	0	42.8	54.6	Cu_2O	cubic
	1	1	1	43.8	67.6	Cu	fcc
	0	0	2	45.1	8.2	Co	hcp
	1	0	1	47.9	0.3	Co	hcp
	0	0	2	50.6	0.1	Cu	fcc
	5	1	1	59.6	12.1	Co_3O_4	cubic
	2	2	0	61.9	35.4	Cu_2O	cubic
	4	4	0	65.3	16.7	Co_3O_4	cubic
	0	2	2	74.4	3.8	Cu	fcc
(v) Co/Cu – AA	1	1	1	36.6	47.9	Cu_2O	cubic
	1	1	1	42.5	100.0	Cu_2O	cubic
	1	1	1	43.5	77.7	Cu	fcc
	0	0	2	50.6	20.2	Cu	fcc
	1	1	3	61.7	57.1	Cu_2O	cubic
	0	2	2	73.8	18.5	Cu	fcc

* hcp = hexagonal close-packed

** fcc = Face-centered cubic

Table S4. Atomic percentages of cobalt, copper, and oxygen atoms in the Co/Cu catalysts as determined by XPS.

Atomic %	**Co**	**Cu**	**O**
(i) Co TF	62.8%	0.0%	37.2%
(ii) Co TF + 0.1 M $CuSO_4$	40.2%	22.1%	37.7%
(iii) Co/Cu – A	20.3%	40.2%	39.5%
(iv) Co/Cu – AA	11.3%	49.7%	39.1%

Table S5. Curve-fitting results of the high-resolution Co 2p XPS spectra of the Co/Cu catalysts. The suggested percentage of Co_3O_4 and $Co(OH)_2$, and the curve-fit residual standard deviation (Residual STD).

Area %	**Co_3O_4**	**$Co(OH)_2$**	**Residual STD**
(i) Co TF	53.0%	47.0%	2.46
(ii) Co TF + 50 µL CuSO4	10.3%	89.7%	1.34
(iii) Co/Cu – A	0%	100%	1.30
(iv) Co/Cu – AA	0%	100%	1.15

Table S6. Curve-fitting results of the high-resolution Cu 2p XPS spectra of the Co/Cu catalysts. The suggested percentage of Cu(0)+Cu(I) and Cu(II) oxidation states, and the curve-fit residual standard deviation (Residual STD).

Area %	**Cu(0) + Cu(I)**	**Cu(II)**	**Residual STD**
(iii) Co/Cu – A	45.7%	54.3%	1.79
(iv) Co/Cu – AA	42.1%	57.9%	1.15

Table S7. Faradaic efficiencies (%) of formate and carbon monoxide at applied potential from -0.4 to -0.9 V vs. RHE using Co/Cu – A and Co/Cu – AA catalysts.

Co/Cu – A				
E (V vs. RHE)	$FE_{formate}$%	FE_{CO} %	Formate Yield (mmol/h)	CO Yield (mmol/h)
-0.4	28.56	24.25	1.65	1.20
-0.5	22.20	34.65	2.03	1.94
-0.6	16.81	51.30	2.15	2.05
-0.7	10.85	59.46	1.81	2.36
-0.8	7.82	57.66	1.63	3.53
-0.9	6.27	57.64	1.60	4.85

Co/Cu – AA				
E (V vs. RHE)	$FE_{formate}$%	FE_{CO} %	Formate Yield (mmol/h)	CO Yield (mmol/h)
-0.4	31.65	44.54	2.19	0.85
-0.5	20.37	48.64	2.47	1.20
-0.6	13.92	52.34	2.41	2.34
-0.7	8.66	58.11	2.11	3.06
-0.8	5.05	66.62	1.59	6.65
-0.9	3.93	74.36	1.54	8.24

Table S8. Comparison of related Co- and Cu-based catalysts for the electrochemical reduction of CO_2 recently reported in the literature.

Catalyst	Potential	Cathodic Current density (mA/cm^2)	$FE_{Formate}$ %	FE_{CO} %	Ref.
Co nanodendrites	-0.4 V *vs. RHE*	73	49.5	n/a	[9]
Single-unit-cell layers of Co_3O_4	-0.87 V *vs. RHE*	2.7	87.6	~10	[10]
4 atomic layers of partially oxidized Co	-0.85 V *vs. SCE*	10.59	90.1	n/a	[11]
1.72 nm thick Co_3O_4 layer	-0.88 V *vs. SCE*	0.68	64.3	n/a	[12]
Co_3O_4 nanofibers	-1.5 V *vs. RHE*	0.5	27.0	65.0	[13]
Co_3O_4 nanocubes on N-doped graphene ($NG\text{-}Co_3O_4\text{-}30$)	-0.95 V *vs. SCE*	10.50	83.0	n/a	[14]
Flower-like Co	-0.85 V *vs. SCE*	~0.5	63.4	n/a	[15]
Cu nanodendrites	-0.4 V *vs. RHE*	2.93	n/a	n/a	[16]
Cu nanopores	-0.6 V vs. RHE	-15	48.2	43.0	[17]
$Cu_{90}Co_{10}$ nanoparticles	-1.1 V *vs. RHE*	3	~10	~7	[18]
Co-decorated Cu Thin Film (CuCo-650-400)	-0.65 V *vs. RHE*	-0.81	~80	n/a	[19]
Co/Cu – A	-0.4 V *vs.* RHE	-31.36	28.14	24.25	This Work
	-0.7 V *vs.* RHE	-89.20	10.92	59.46	
Co/Cu – AA	-0.4 V *vs.* RHE	-37.01	31.30	44.54	This Work
	-0.9 V *vs.* RHE	-220.90	4.02	74.36	

References:

1 M. C. Biesinger, B. P. Payne, A. P. Grosvenor, L. W. M. Lau, A. R. Gerson and R. S. C. Smart, *Appl Surf Sci*, 2011, **257**, 2717–2730.

2 M. C. Biesinger, L. W. M. Lau, A. R. Gerson and R. S. C. Smart, *Appl Surf Sci*, 2010, **257**, 887–898.

3 M. C. Biesinger, *Surface and Interface Analysis*, 2017, **49**, 1325–1334.

4 J. S. Dondapati, A. R. Thiruppathi, A. Salverda and A. Chen, *Electrochem commun*, 2021, **124**, 106946.

5 G. Marcandalli, M. C. O. Monteiro, A. Goyal and M. T. M. Koper, *Acc Chem Res*, 2022, **55**, 1900–1911.

6 M. König, J. Vaes, E. Klemm and D. Pant, *iScience*, 2019, **19**, 135–160.

7 J. Y. Ye, Y. X. Jiang, T. Sheng and S. G. Sun, *Nano Energy*, 2016, **29**, 414–427.

8 R. Kas, O. Ayemoba, N. J. Firet, J. Middelkoop, W. A. Smith and A. Cuesta, *ChemPhysChem*, 2019, **20**, 2904–2925.

9 S. Abner and A. Chen, *Appl Catal B*, 2022, **301**, 120761.

10 S. Gao, Z. Sun, W. Liu, X. Jiao, X. Zu, Q. Hu, Y. Sun, T. Yao, W. Zhang, S. Wei and Y. Xie, *Nat Commun*, 2017, **8**, 1–9.

11 S. Gao, Y. Lin, X. Jiao, Y. Sun, Q. Luo, W. Zhang, D. Li, J. Yang and Y. Xie, *Nature*, 2016, **529**, 68–71.

12 S. Gao, X. Jiao, Z. Sun, W. Zhang, Y. Sun, C. Wang, Q. Hu, X. Zu, F. Yang, S. Yang, L. Liang, J. Wu and Y. Xie, *Angewandte Chemie - International Edition*, 2016, **55**, 698–702.

13 A. Aljabour, H. Coskun, D. H. Apaydin, F. Ozel, A. W. Hassel, P. Stadler, N. S. Sariciftci and M. Kus, *Appl Catal B*, 2018, **229**, 163–170.

14 P. Sekar, L. Calvillo, C. Tubaro, M. Baron, A. Pokle, F. Carraro, A. Martucci and S. Agnoli, *ACS Catal*, 2017, **7**, 7695–7703.

15 G. Yang, Z. Yu, J. Zhang and Z. Liang, *Cuihua Xuebao/Chinese Journal of Catalysis*, 2018, **39**, 914–919.

16 M. Nur Hossain, S. Chen and A. Chen, *Appl Catal B*, 2019, **259**, 118096.

17 A. Salverda, S. Abner, E. Mena-Morcillo, A. Zimmer, A. Elsayed and A. Chen, *Journal of Physical Chemistry C*, 2023, **127**, 7151–7161.

18 M. Bernal, A. Bagger, F. Scholten, I. Sinev, A. Bergmann, M. Ahmadi, J. Rossmeisl and B. R. Cuenya, *Nano Energy*, 2018, **53**, 27–36.

19 C. Dai, L. Sun, J. Song, H. Liao, A. C. Fisher and Z. J. Xu, *Small Methods*, 2019, **3**, 1–7.